King's Research Portal

DOI:
10.1002/aenm.202002387

Document Version
Publisher's PDF, also known as Version of record

Link to publication record in King's Research Portal

Citation for published version (APA):
Huang, C., Leung, C. L. A., Leung, P., & Grant, P. S. (2021). A Solid-State Battery Cathode with a Polymer Composite Electrolyte and Low Tortuosity Microstructure by Directional Freezing and Polymerization. *Advanced Energy Materials*, *11*(1), [2002387]. https://doi.org/10.1002/aenm.202002387

Citing this paper
Please note that where the full-text provided on King's Research Portal is the Author Accepted Manuscript or Post-Print version this may differ from the final Published version. If citing, it is advised that you check and use the publisher's definitive version for pagination, volume/issue, and date of publication details. And where the final published version is provided on the Research Portal, if citing you are again advised to check the publisher's website for any subsequent corrections.

General rights
Copyright and moral rights for the publications made accessible in the Research Portal are retained by the authors and/or other copyright owners and it is a condition of accessing publications that users recognize and abide by the legal requirements associated with these rights.

- Users may download and print one copy of any publication from the Research Portal for the purpose of private study or research.
- You may not further distribute the material or use it for any profit-making activity or commercial gain
- You may freely distribute the URL identifying the publication in the Research Portal

Take down policy
If you believe that this document breaches copyright please contact librarypure@kcl.ac.uk providing details, and we will remove access to the work immediately and investigate your claim.

Download date: 06. Oct. 2023

A Solid-State Battery Cathode with a Polymer Composite Electrolyte and Low Tortuosity Microstructure by Directional Freezing and Polymerization

Chun Huang, Chu Lun Alex Leung, Puiki Leung, and Patrick S. Grant**

Solid-state Li metal batteries (SSLMBs) combine improved safety and high specific energy that can surpass current Li ion batteries. However, the Li$^+$ ion diffusivity in a composite cathode—a combination of active material and solid-state electrolyte (SSE)—is at least an order of magnitude lower than that of the SSE alone because of the highly tortuous ion transport pathways in the cathode. This lowers the realizable capacity and mandates relatively thin (30–300 µm) cathodes, and hence low overall energy storage. Here, a thick (600 µm) hybrid cathode comprising vertically aligned $LiNi_{0.8}Mn_{0.1}Co_{0.1}O_2$ (NMC811)-rich channels filled with a [LiTFSI+PEGMA+MePrPyl TFSI] polymer composite electrolyte is fabricated by an innovative directional freezing and polymerization method. X-ray micro-computed tomography, ion mobility simulations, and DC depolarization show that the cathode structure improves Li$^+$ ion diffusivity in the cathode from 4.4×10^{-9} to 1.4×10^{-7} cm^2 s^{-1}. In a SSLMB full cell at 25 °C, the cathode provides gravimetric capacities of 199 and 120 mAh g^{-1}, and ultra-high areal capacities of 16.7 and 10.1 mAh cm^{-2} at 0.05 and 1 C, respectively. The work demonstrates a scalable approach to realizing composite cathode structures with kinetically favorable ion transport characteristics in SSLMBs.

1. Introduction

Rechargeable batteries that provide increased specific energy and improved safety over commercial Li ion batteries (LIBs) are in demand for applications such as electric vehicles (EVs), all-electric aircraft and the grid-scale storage of electricity from renewable but intermittent electricial generation.[1] Most commercial LIBs use a graphite anode (theoretical capacity 372 mAh g^{-1}, electrochemical potential −0.43 V versus standard hydrogen electrode).[2] Although graphite is relatively low cost and easy to process into electrodes at large scale, a switch to a Li metal anode would provide a theoretical capacity of 3860 mAh g^{-1} and a lower electrochemical potential (−3.04 V versus standard hydrogen electrode).[3] When a Li metal anode is coupled with a high capacity cathode (e.g., $LiNi_{0.8}Mn_{0.1}Co_{0.1}O_2$ (NMC811)), the resulting battery would approximately double specific energy from 250 to 300 Wh kg^{-1} for commercial LIBs to ≈500 Wh kg^{-1}.[4–6] However, a Li metal anode is unstable with conventional liquid electrolytes (which are also flammable) and Li dendrites formed during cycling may readily penetrate through standard porous olefin separators and cause short circuits, rapid discharge, and a range of subsequent safety hazards.[7]

Solid-state Li metal batteries (SLMBs) use a solid-state electrolyte (SSE) to replace the liquid electrolyte and separator, and alongside capacity improvements, also have the potential to enable safer cycling, although achieving practical current densities remains a significant challenge.[8] Compared with the high ionic conductivity of liquid electrolytes (10^{-3}–10^{-2} S cm^{-1} at room temperature, RT), SSEs usually have much lower intrinsic ionic conductivities at RT,[9] and most SSLMB research has therefore focused on increasing the ionic conductivity of SSEs. The SSEs divide into two main families: inorganic electrolytes and polymer electrolytes.[10] Inorganic electrolyte types include NASICON,[11–13] garnet,[14–16] perovskite,[17–19] LISICON,[20] sulfide,[21–24] argyrodite,[25–27] glassy,[9] etc. Inorganic electrolytes typically have ionic conductivities of 2×10^{-5} to 2×10^{-3} S cm^{-1} at RT. Practical applications have been limited by manufacturing difficulties (fragility over large areas), poor electrode/SSE interfacial contact, and risk of Li dendrite growth along grain boundaries, although steady progress is being made.[10] In most polymer electrolytes, Li$^+$ ionic conductivity is achieved by

Dr. C. Huang
Department of Engineering
King's College London
London WC2R 2LS, UK
E-mail: ann.huang@kcl.ac.uk

Dr. C. Huang, Prof. P. S. Grant
Department of Materials
University of Oxford
Oxford OX1 3PH, UK
E-mail: patrick.grant@materials.ox.ac.uk

Dr. C. L. A. Leung
Department of Mechanical Engineering
University College London
London WC1E 7JE, UK

Dr. C. L. A. Leung
Research Complex at Harwell
Rutherford Appleton Laboratory
Didcot OX11 0FA, UK

Dr. P. Leung
Faculty of Engineering and the Environment
University of Southampton
Southampton SO17 1BJ, UK

The ORCID identification number(s) for the author(s) of this article can be found under https://doi.org/10.1002/aenm.202002387.

DOI: 10.1002/aenm.202002387

the solvation of a Li salt such as lithium hexafluorophosphate ($LiPF_6$) or lithium bis(trifluoromethanesulfonyl)imide (LiTFSI) in a polymer matrix. Polymer electrolyte types include solid polymer-only[28] and ionic polymers.[29] Poly(ethylene oxide) (PEO),[30] poly(acrylonitrile) (PAN),[31] poly(methyl methacrylate) (PMMA),[32] poly(vinyl alcohol) (PVA),[33] and poly(propylene) oxide (PPO)[34] are commonly used as solid polymer-only electrolytes, but their ionic conductivity (2×10^{-5} to 2×10^{-4} S cm^{-1} at RT[35,36]) is relatively low. Ionic polymers that solidify a cation–anion pair (e.g., from an ionic liquid, IL) into a polymer matrix are attractive because ILs have negligible vapor pressure, high electrochemical stability, and excellent thermal resistance.[37,38] ILs can increase the ionic conductivity to 2 to 4×10^{-4} S cm^{-1} at RT[29,39] because the number of Li^+ conduction sites along the polymer backbone is increased and polymer crystallization is suppressed.[40] The resulting ionic polymers have a much higher entropy and free volume for polymer segmental motion of the Li^+ conduction sites.[41] Other advantages of ionic polymer electrolytes include compatibility with large-scale manufacturing processes, good electrode/SSE interfacial contact, and high toughness that can either help to slow Li dendrite formation[5] or buffer the elastic deformation caused by the Li front movement to prevent dendrite penetration.[42]

Alongside research to increase the intrinsic ionic conductivity of SSEs, there is a growing interest in tailoring the electrode and cell structure at a range of length-scales. For example, at the sub-particle scale through particle grading and coating[43,44] and at the electrode scale through grading, layering, etc.[13,45]. In the case of SSLMB anodes, this has been explored to improve the uniformity of Li plating on charging and to buffer Li volume changes, for example, using Ag–C composite interlayers,[6] 1D Cu/C pillars,[46] 2D graphene/MXene,[47] 3D Cu,[48] and 3D C frameworks.[49]

SSLMB cathodes usually comprise a randomly mixed microstructure of electrochemically active and SSE materials in which the SSE forms a highly tortuous percolating network for Li^+ transport (**Figure 1**a). Combined with the low intrinsic ionic conductivity of most SSEs, this tortuous ion transport network leads to limited ion transport,[50–54] a steep Li^+ ion concentration gradient across the cathode thickness, and ion starvation in some regions,[55–57] significantly hindering overall cell performance.[58,59] Further, in order for the cathode capacity to match the high capacity of the Li metal anode (5–10 µm), modeling suggests that the cathode thickness should increase from typically $\leqslant$300 µm to 600 µm.[8] Unfortunately, the increased thicknesses only amplify the Li^+ transport restrictions and reduce even further the achievable cell capacity.

Most SSLMB cathodes are manufactured by doctor-blade coating of a mixture of active, SSE and sometimes C electrical conductive additives and binder, usually followed by heating and/or pressing.[60,61] Some approaches dispense with C electrical conductive additives, for example, if the active material is C coated, but can still exhibit adequate electrochemical performance (e.g., 107–152 mAh g^{-1} at 0.1 C),[8,62–64] because in these configurations Li^+ transport rather than electron percolation is the limiting factor on SSLMB performance.[65,66] Doctor-blade coating of a porous cathode followed by infiltrating of an SSE ("back-filling") is also used,[67] but the cathode tortuous pore network cannot be easily infiltrated (only >2 µm pores can be effectively infiltrated with SSE[68]) and leads to poor active material/SSE contact and a high interfacial resistance.

To reduce the randomness of the ion pathways, anisotropic transport networks have been contrived using sacrificial pore formers, or templates. Most of these template methods have focused on the SSE membrane only (not the composite cathode), for example, 3D printing of an insulating sacrificial polymer template followed by infiltration of a $Li_{1.4}Al_{0.4}Ge_{1.6}(PO_4)_3$ (LAGP) SSE then removal of the sacrificial template through heating, and finally back-filling the LAGP framework with polypropylene (PP) to provide structural stabilization.[69] These templating approaches require several discrete processing steps, including removal of the sacrificial template using high temperature (600–900 °C) or chemical reagents that may either damage the active materials or place severe constraints on the choice of materials.[70]

Here, we synthesize a new ionic polymer electrolyte composed of the conducting salt LiTFSI and IL 1-methyl-1-propylpyrrolidinium bis(trifluoromethanesulfonyl)imide (MePrPyl TFSI) solidified in a poly(ethylene glycol) methacrylate (PEGMA) matrix. We then fabricate a 600 µm thick cathode comprising vertically aligned NMC811-rich pillars surrounded by the ionic polymer electrolyte in a single step, with no templating required (Figure 1b). These hybrid cathodes are fabricated using an innovative directional freezing and polymerization (DFP) process in which active cathode particles and ionic polymer are self-assembled directly into a preferred anisotropic and dense cathode structure, with no need for any subsequent pressing, heating, SSE infiltration, or template removal steps. The [LiTFSI+PEGMA+MePrPyl TFSI] after polymerization has a competitive ionic conductivity of 4.2×10^{-4} S cm^{-1} at 25 °C. Critically, the DFP method produces an intimate active/SSE interfacial contact. We combine X-ray micro-computed tomography (microCT) and Li^+ ion transport simulations to show that ion conduction pathway tortuosity is reduced from 3.3 to 4.9 for standard SSLMB composite cathodes[71] to 1.2 for the cathode made by DFP. DC depolarization shows that the effective ion diffusivity in the same cathode is increased from 4.4×10^{-9} to 1.4×10^{-7} cm^2 s^{-1}. An SSLMB using the cathode exhibits a near theoretical gravimetric capacity of 199 mAh g^{-1} and an ultra-high areal capacity of 16.7 mAh cm^{-2} at 0.05 C, and 120 mAh g^{-1} (10.1 mAh cm^{-2}) at 1 C at RT, which are amongst the highest reported at the same testing conditions. To the best knowledge of the authors, the work is amongst the first to report non-templated vertically aligned cathode structures with fast Li^+ transport kinetics for SSLMBs. The DFP method should be applicable to a wide range of electrode materials.

2. Results and Discussion

2.1. Directional Freezing and Polymerization

Figure 1c shows a schematic diagram of the DFP process. A suspension was first prepared containing NMC811 particles, LiTFSI conducting salt, PEGMA monomer solution, MePrPyl TFSI IL, and 1-hydroxycyclohexyl phenyl ketone-based Irgacure

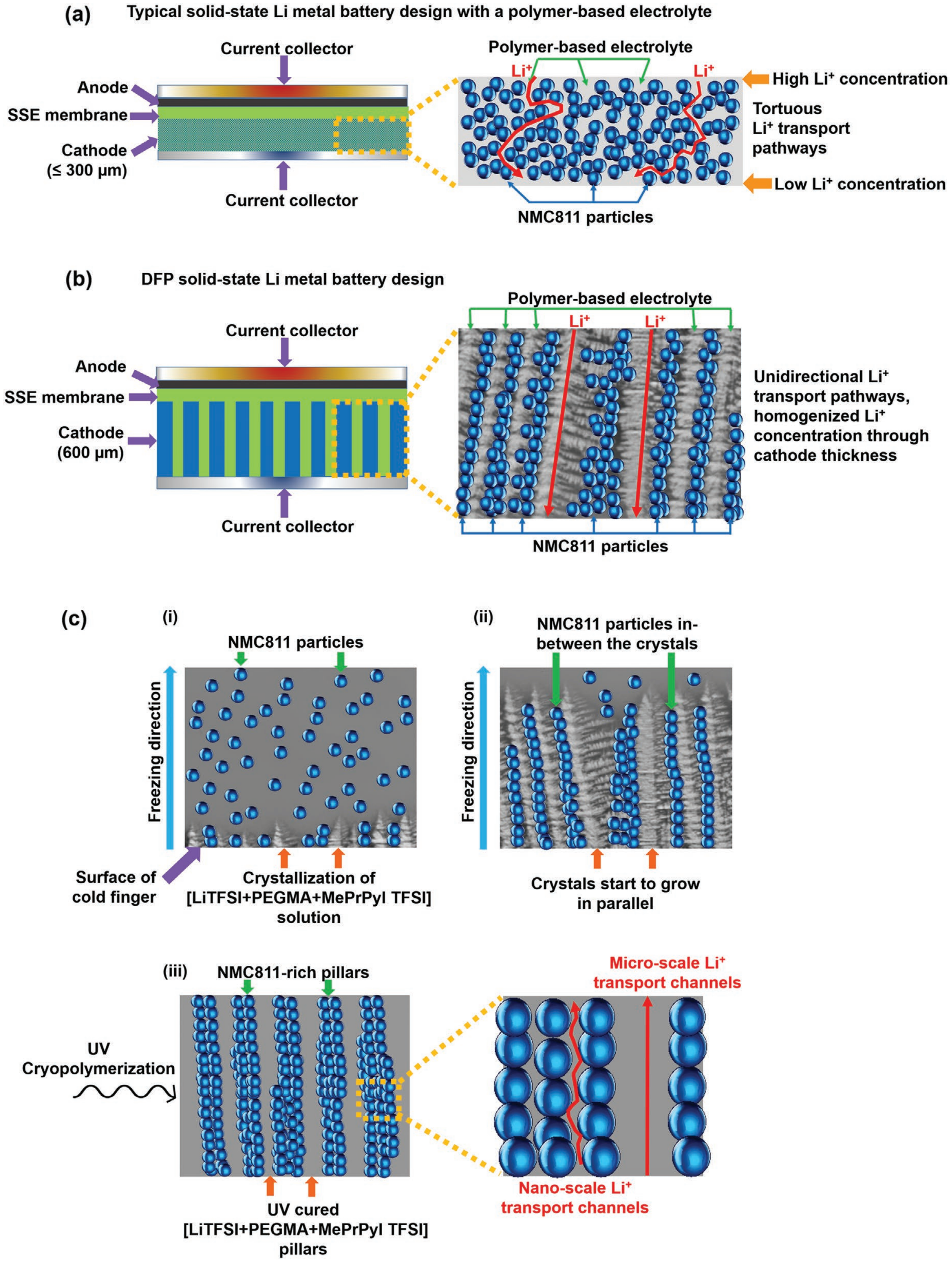

Figure 1. Schematic diagrams of a) a typical solid-state Li metal battery (SSLMB) design that uses a polymer-based electrolyte with a randomly mixed cathode structure (⩽300 µm thick) involving tortuous percolative Li^+ ion transport pathways through the inter-connected SSE; b) the SSLMB design with an anisotropic cathode structure (600 µm thick) comprising vertically aligned NMC811-rich pillars surrounded by a polymer-based electrolyte; and c) the steps of the directional freezing and polymerization (DFP) process to fabricate the anisotropic cathode structure, showing the micro- and nano-scale Li^+ ion transport channels.

photoinitiator. The suspension was then directionally frozen in the vertical direction, "bottom to top" at a controlled freezing rate of 2 mm min^{-1}. Supercooled clusters of PEGMA monomer and MePrPyl TFSI molecules crystallized.[72] Because heterogeneous crystal nucleation at a foreign surface has a lower free energy barrier than homogeneous nucleation directly from solution, the PEGMA and MePrPyl TFSI crystals were first formed on the surface of the cold finger at −30 °C[73] (Figure S1, Supporting Information shows a schematic of the DFP apparatus). As the solution of [LiTFSI+PEGMA+MePrPyl TFSI] continued to freeze, the crystals grew parallel to the strong vertical temperature gradient, and self-assembled into a vertically aligned structure spanning hundreds of micrometers that pushed the NMC811 particles sideways into the regions in-between the growing crystal pillars. On subsequent in-situ UV cryopolymerization at −25 °C, the [LiTFSI+PEGMA+MePrPyl TFSI] solidified with the PEGMA acting as the host polymer matrix for cross-linking with the MePrPyl TFSI.[74] UV polymerization is usually associated with thinner layers (50-100 µm) but UV polymerization of thicker layers (100 µm–2.5 mm) can be achieved by increasing irradiance intensity and exposure duration,[75] for example, 1.4 mm thick methacrylate films[76] and 800 µm thick polyethylene films containing LiTFSI, ethoxylated trimethylolpropane triacrylate (ETPTA), and succinonitrile (SN)[77] were cured at 300–800 mW cm^{-2} for 120 s–60 min. Here, an irradiance intensity of 400 mW cm^{-2} and exposure duration of 40 min were used, which as shown later, fully cured the 600 µm thick cathode structures into vertically aligned NMC811-rich pillars with the interstices between the pillars filled with dense [LiTFSI+PEGMA+MePrPyl TFSI]. All the functional materials in the suspension were directly incorporated into the final cathode structure and no subsequent pressing, heating, template material removal, or SSE back-filling steps of any type were required.

The anisotropic cathode structural design was intended to provide micro-scale, low tortuosity SSE pathways in-between the vertical NMC-rich pillars and fast Li$^+$ ion transport through the hybrid cathode thickness, while SSE incorporated within the NMC-rich pillars themselves would facilitate nano-scale transport of ions to each NMC particle. It was also intended that the C-coated NMC-rich pillars would provide sufficient electrical conductivity along the pillars that the addition of electrical conductive additives could be avoided, which has already been shown for anisotropic $LiCoO_2$ cathodes made by co-extrusion[78] and by magnetic templating,[79] and for $LiNi_{0.8}Co_{0.15}Al_{0.05}O_2$ cathodes by freeze casting.[80] Note that the polymer-based SSE also provided mechanical stabilization of the cathode structure and there was no need for any additional inactive component such as a binder.

Figure S2, Supporting Information shows a photo of the resulting hybrid cathode with excellent structural integrity that enabled easy handling, in this case simply using a pair of tweezers. The mechanical strength of a polymer composite containing the same MePrPyl TFSI used here at an IL : polymer volume ratio of 1 : 1 was investigated by tensile testing at a speed of 1 cm min^{-1}, giving a tensile strength of 6.7 MPa and an elongation of 178% at room temperature.[81] Mechanical strength was improved on reducing the IL:polymer volume ratio to 0.5:1.[82] Although the addition of IL decreased the glass transition temperature of the composite, the strong ion–dipole interaction between the dissociated Li$^+$ cation from LiTFSI and ether oxygen from PEGMA contributed to mechanical stability, even up to 40 °C.[83] Further improvement in mechanical stability at elevated temperatures $\geqslant$60 °C has been investigated through i) a higher degree of cross linking (e.g., by adding a polymerizable IL 1,4-di(vinylimidazolium)butane bisbromide[84]) and ii) adding nanoparticles such as Al_2O_3 to promote physical entanglements between the nanoparticles and polymer backbone.[85]

To make an SSLMB full cell, a mixed solution of LiTFSI, MePrPyl TFSI, PEGMA monomer, and photoinitiator was directly drop cast onto the composite cathode followed by the same in situ UV cryopolymerization process to make a ≈150 µm thick SSE membrane. A Li metal foil as the anode was then added onto the SSE membrane. The arrangement was assembled into a coin cell that provided moderate compression to ensure sustained and reproducible contact of the electrode/SSE interfaces.

Other than the hybrid cathode made by DFP with the ionic polymer already described, termed [DFP+IP], to investigate the effect of SSE and differences in cathode structure on electrochemical properties, two other types of hybrid cathode were fabricated: i) using [LiTFSI+PEGMA] SSE without MePrPyl TFSI made by directional freezing and polymerization, termed [DFP+P], and ii) again using the [LiTFSI+PEGMA+MePrPyl TFSI] SSE but now with isotropic freezing and polymerization, termed [IFP+IP]. All the cathodes contained the same proportion (62 ± 5 vol%) of NMC811 active material, and similar to 40–60 vol% active material used in the majority of cathodes for SSLMBs.[8,86,87] A summary of the materials, average cathode thickness and active material mass loading for the three types of cathode is given in **Table 1**.

Table 1. Summary of the different cathode fabrication routes, materials, thickness, and mass loading.

Fabrication method	Materials	Freezing direction	SSE integrated in fabrication?	Thickness [µm]	Mass loading [mg cm^{-2}]
Directional freezing and polymerization with ionic polymer (DFP+IP)	NMC811, LiTFSI, PEGMA, and MePrPyl TFSI	Unidirectional	Yes	600	83.9
Directional freezing and polymerization with polymer only (DFP+P)	NMC811, LiTFSI, and PEGMA	Unidirectional	Yes	600	75.6
Isotropic freezing and polymerization with ionic polymer (IFP+IP)	NMC811, LiTFSI, PEGMA, and MePrPyl TFSI	Isotropic	Yes	600	82.2

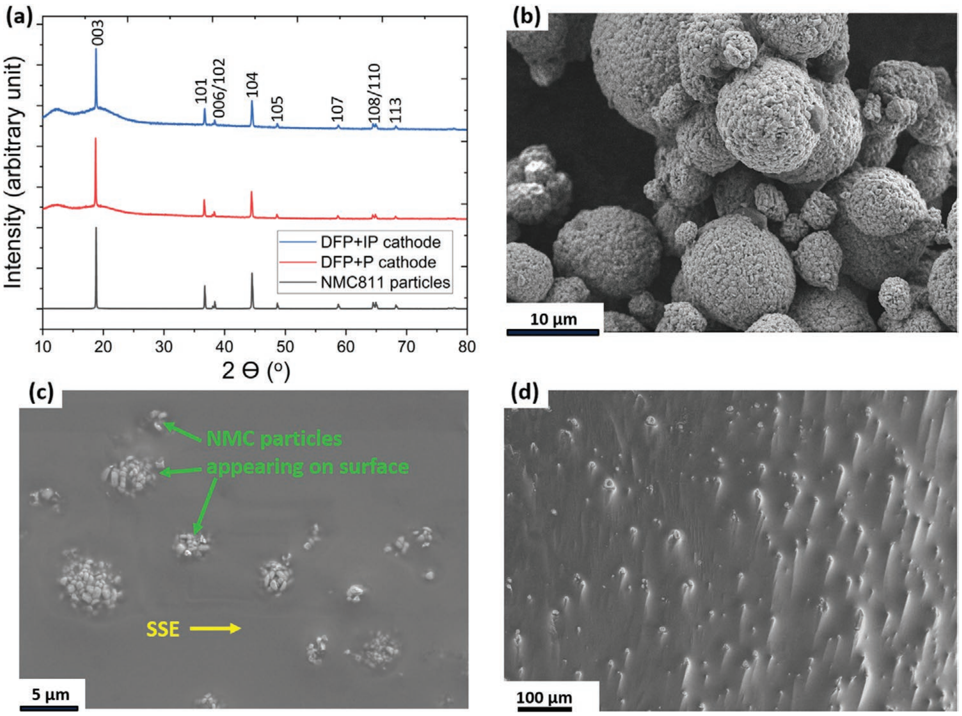

Figure 2. a) X-ray diffraction (XRD) patterns of NMC811 feedstock powder, a directional freezing and polymerization with polymer only [DFP+P] cathode and a directional freezing and polymerization with ionic polymer [DFP+IP] cathode; scanning electron microscopy (SEM) images of b) NMC811 particles, c) the upper surface, and d) a cross section of the as-fabricated [DFP+IP] cathode.

2.2. Vertically Aligned Cathode Structure

Figure 2a shows X-ray diffraction (XRD) patterns of the NMC811 feedstock powder and the [DFP+P] and [DFP+IP] cathodes. The split peaks of (006)/(102) and (108)/(110) reflections (magnified in Figure S3a–c, Supporting Information) in all three patterns was the typical structure of a close-packed oxygen lattice with alternating layers of Li^+ and transition metal ions in an octahedral coordination configuration.[88,89] All of the reflections readily indexed to $LiNi_{0.8}Mn_{0.1}Co_{0.1}O_2$ with a $R\bar{3}m$ space group[90] i.e. there were no additional chemical or material phase changes caused by fabrication. Figure S4, Supporting Information shows differential scanning calorimetry (DSC) traces of the NMC811 feedstock powder and the [DFP+P] and [DFP+IP] cathodes. There were no sharp endothermic (melting) peaks suggesting good thermal stability and no significant phase separation in the range –85 to 300 °C.[91]

Figure 2b shows a scanning electron microscopy (SEM) image of the NMC811 feedstock particles (and a magnified individual NMC811 particle in Figure S5, Supporting Information), with typical 4–17 µm spherical secondary particles consisting of 200–700 nm primary particles.[92] Figure S6, Supporting Information is a transmission electron microscopy (TEM) image of the edge of a NMC811 particle showing a ≈8 nm thin C coating because the NMC811 was synthesized in the presence of oxygen at high calcination temperature (800 °C) where organic reagents reacted to leave a carbonaceous film with useful electrical conductivity.[93–95]

Figure 2c shows a plan view SEM image of the dense upper free surface of the [DFP+IP] cathode after polymerization (a larger area electrode plan view SEM image is given in Figure S7, Supporting Information). Figure 2d shows a corresponding cross-sectional SEM image of the [DFP+IP] cathode after polymerization. Both SEM images show full densification of the polymeric matrix across the entire 600 µm thickness, and the cured [LiTFSI+PEGMA+MePrPyl TFSI] SSE readily wetted onto the NMC811 particles and filled the interparticulate interstices within the NMC-rich pillars. High density (⩾95%) is considered crucial for useful rates of Li^+ ion transport in the cathodes of solid-state batteries.[96] In contrast, a similar SEM image of the [DFP+P] cathode after polymerization in Figure S8, Supporting Information shows 800 nm–4 µm pores, indicating that polymerization shrinkage was developed after curing.[97] These results indicate that the addition of MePrPyl TFSI to the [DFP+IP] cathode suppressed PEGMA crystallinity[98] and eliminated the tendency for shrinkage pores.[74,99]

To investigate the effects of directional freezing on the cathode structure, cross sections of the [IFP+IP] and [DFP+IP] hybrid cathodes were prepared for SEM by Ar^+ ion etching to gently and preferentially remove some of the SSE. **Figure 3**a is a resulting cross-sectional SEM image of the [IFP+IP] cathode after ion etching, showing a pattern of similar-sized (≈0.8 µm) circular “dimples” with no obvious long range alignment or directionality. In contrast in Figure 3b, and consistent with Figure 2d, the [DFP+IP] cathode showed a distinct vertically aligned structure with larger NMC811 secondary particles exposed on the top of the majority of the NMC-rich pillars, suggesting that the pillar growth (during freezing) was stopped when encountering a particularly large NMC secondary particle.

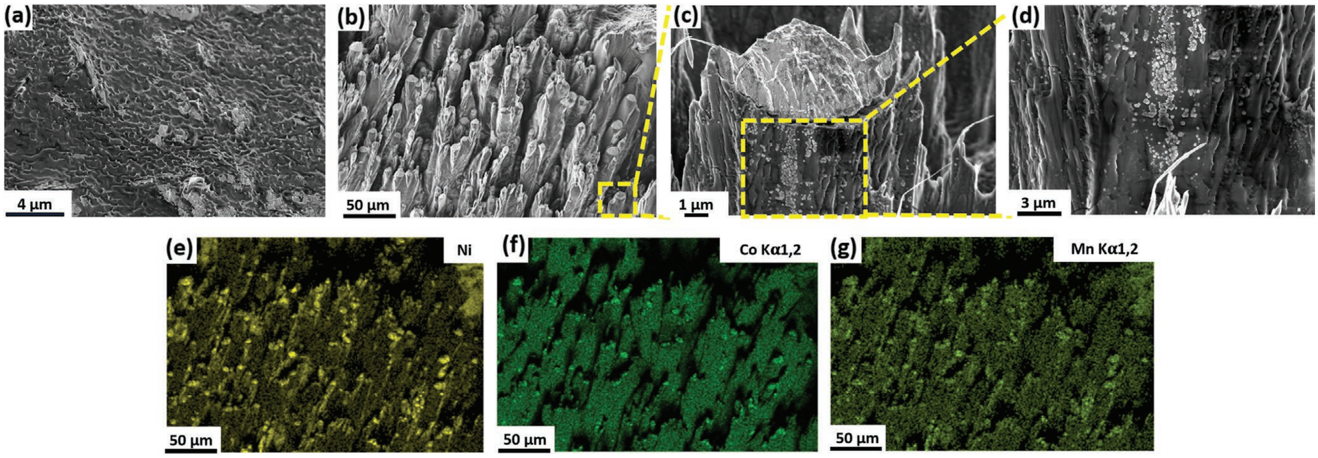

Figure 3. Cross-sectional SEM images of a) an [IFP+IP] cathode, and b) a [DFP+IP] cathode, c,d) magnified cross-sectional SEM images of a pillar from the [DFP+IP] cathode, and e–g) energy dispersive X-ray spectroscopy (EDS) maps for Ni, Co, and Mn from the [DFP+IP] cathode. All electrodes were prepared after Ar^+ ion etching.

Figure 3c,d shows magnified cross-sectional SEM images of a pillar with embedded smaller (200–700 nm) NMC811 primary particles. Figure 3e–g shows energy dispersive X-ray spectroscopy (EDS) maps for Ni, Co, and Mn, respectively, confirming that the NMC811 particles were incorporated and concentrated within the pillar-like structures. Furthermore, Figure S9, Supporting Information shows the cross-sectional SEM image of the [DFP+IP] cathode after 200 charge and discharge cycles (cycling performance described later) and after the battery was dissembled, showing that the aligned anisotropic electrode structure was maintained and confirming the mechanical stability of the cathode structure.

2.3. Electrochemical Stability and Ionic Conductivity of the Polymer-Based SSE

A wide battery operating voltage window is advantageous for increasing the specific energy and is often determined by the electrochemical stability of the SSE for a SSLMB.[8] To investigate the relative stability of the SSE computational density functional theory (DFT) calculations were used. The geometric structure of the PEGMA molecular unit cross-linked with a $[MePrPyl]^+$ cation and a $[TFSI]^-$ anion was first obtained (**Figure** 4a), and the electron density distribution during redox reactions then investigated. The highest occupied molecular orbital (HOMO) and the lowest unoccupied molecular orbital (LUMO) of the molecule were calculated. In general, the stability window between upper and lower potentials for oxidation and reduction processes has a linear correlation with the energy difference between HOMO and LUMO.[43,100,101] Figure 4b shows the calculated HOMO band of the cross-linked molecule. The contours indicate the extent to which regions have a tendency to be oxidized, in this case located principally on the $[TFSI]^-$ anion due to its electron-rich regions around the oxygen and sulfur atoms in the sulfonyl groups.[102] Hence, the resistance of $[TFSI]^-$ to oxidation determines the upper potential limit of the cross-linked molecule. Figure 4c shows the calculated LUMO band of the same molecule, with contours now indicating the extent to which the region has a tendency to be reduced, located on the PEGMA unit due to its reactive hydroxyl group that gains an extra electron.[103] Hence, the resistance of the PEGMA unit to reduction determines the lower potential limit of the cross-linked molecule. Figure S10, Supporting Information shows the estimated HOMO and LUMO for the separate molecular structures of a PEGMA unit and a MePrPyl TFSI molecule that were consistent with those of the cross-linked molecule.

The HOMO and LUMO of some of the other common polymer units and IL molecules were also calculated and are summarized in Figure 4d. The energy difference for PEGMA is 6.34 eV and higher than some of the other common polymer electrolytes such as PAN (6.18 eV) and PPO (6.22 eV). The energy difference for MePrPyl TFSI was 5.90 eV and higher than some of the other common ILs such as BuMeIm TFSI (5.72 eV) and *N*,*N*-diethyl-2-methoxy-*N*-methylethanamonium tetrafluoroborate (DeMe BF_4, 5.74 eV).[104] Further, the energy difference for the cross-linked [PEGMA + MePrPyl TFSI] molecule was 6.43 eV and higher than either of PEGMA or MePrPyl TFSI on its own, confirming that cross-linking increased electrochemical stability due to the strong electrostatic interactions between the $[MePrPyl]^+$ cation, $[TFSI]^-$ anion and the OH^- group of PEGMA.[105,106]

To investigate the potential stability of the SSE against a Li metal anode, Figure S11, Supporting Information is a linear sweep voltammogram (LSV) between −3.2 and 5.6 V in a stainless steel (SS)/SSE/Li cell configuration showing anodic and cathodic stability limits of 4.7 and −2.9 V, respectively, and an overall potential stability window of 7.6 V. This window is larger than some of the other SSEs such as PEO (≈4.5 V)[107] and other high voltage cathode materials such as NMC811 (upper voltage ≈4.2 V).[88,108]

To investigate the effects of adding MePrPyl TFSI on ionic conductivity, electrochemical impedance spectroscopy (EIS) was performed in a SS/SSE/SS cell configuration at 25–125 °C (inset of Figure 4e). The ionic conductivity σ was estimated from the equivalent series resistance (R_s) at

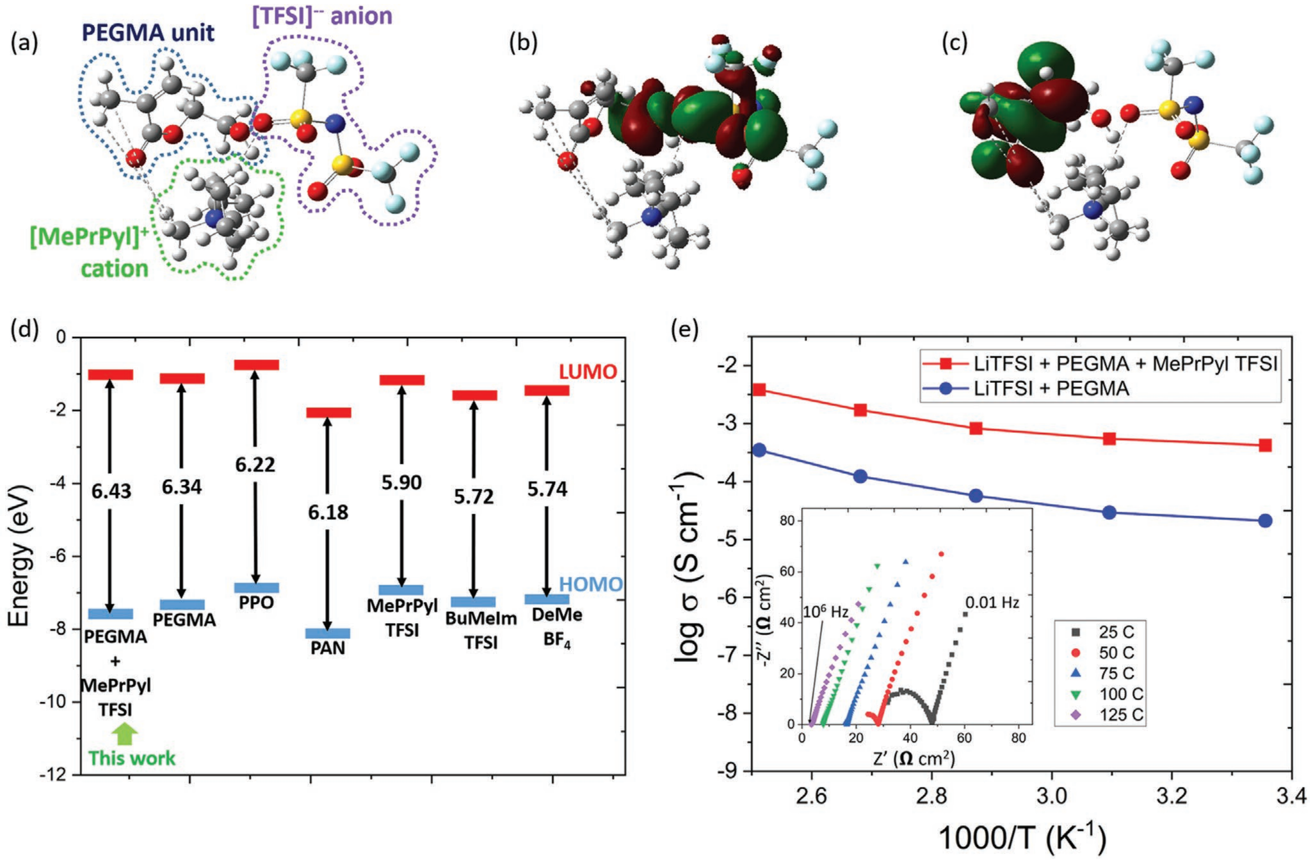

Figure 4. a) The molecular structure of poly(ethylene glycol) methacrylate (PEGMA) cross-linked with a 1-methyl-1-propylpyrrolidinium cation ([MePrPyl]$^+$) and a bis(trifluoromethanesulfonyl)imide anion ([TFSI]$^-$); calculated b) highest occupied molecular orbital (HOMO) and c) lowest unoccupied molecular orbital (LUMO) of the cross-linked molecule; d) a summary of the energy differences for the materials in this work and for some of the other common polymer electrolytes and ionic liquids (ILs) estimated by computational density functional theory (DFT) calculations; and e) experimental results of ionic conductivity of the two types of solid-state electrolyte (SSE): [LiTFSI+PEGMA] and [LiTFSI+PEGMA+MePrPyl TFSI]. Inset: Nyquist plot measured by electrochemical impedance spectroscopy (EIS) for [LiTFSI+PEGMA+MePrPyl TFSI] in a stainless steel (SS)/SSE/SS cell configuration.

the intercept of the Nyquist curve with the real *Z*-axis at the highest frequency and using $\sigma = t/R_sA$ where *t* is the thickness of the SSE and *A* is the contact area.[109,110] Figure 4e summarizes the ionic conductivities showing $\sigma = 4.2 \times 10^{-4}$ S cm^{-1} for [LiTFSI+PEGMA+MePrPyl TFSI] at 25 °C, more than one order of magnitude higher than $\sigma = 2.1 \times 10^{-5}$ S cm^{-1} for [LiTFSI+PEGMA] at the same temperature. The ionic conductivity of 4.2 x 10^{-4} S cm^{-1} at 25 °C was comparable or slightly higher than similar ionic polymers.[29,39–41,111,112] The higher ionic conductivity of [LiTFSI+PEGMA+MePrPyl TFSI] than [LiTFSI+PEGMA] was because Li$^+$ transport mechanism in [LiTFSI+PEGMA] is through association and dissociation of Li$^+$ with the ether oxygen atoms and the negatively charged [OH]$^-$ dipole from PEGMA along the molecular chain using electrostatic interactions[113] whereas the Li$^+$ transport mechanism in [LiTFSI+PEGMA+MePrPyl TFSI] involves the additional association and dissociation of Li$^+$ with the [TFSI]$^-$ anion from MePrPyl TFSI. The good miscibility of MePrPyl TFSI and PEGMA (shown by the DSC results) ensured sufficiently uniform dispersion of [TFSI]$^-$ in the polymer matrix, and MePrPyl TFSI provided PEGMA with a higher degree of local segmental movement.[98]

2.4. Li$^+$ Ion Transport in the Cathode

X-ray micro-computed tomography (microCT) was used to investigate the long-range alignment of the [DFP+IP] cathode structure in 3D. The 3D data volume consisted of a stack of 2D grey-scale image slices and **Figure 5**a shows one 2D image slice with preferential vertical ordering of white and grey phases along the *z*-axis (through the electrode thickness). The 3D data volume was segmented into the different phases based on the different attenuated X-ray intensities that were directly proportional to the phase density (segmentation details in Section 4 and refs. [114,115]). The highest attenuating phase with a density of ≈2.2 g cm^{-3} (red) was the larger (4-17 µm) NMC811 secondary particles. The intermediate attenuating phase with a density of ≈1.7 g cm^{-3} (green) was smaller (2-8 µm) NMC811 particles mixed with a relatively low fraction of SSE (the NMC-rich pillars). The lowest attenuating phase with a density of ≈1.2 g cm^{-3} (blue) was the SSE alone. Not all of the smaller NMC811 primary particles could be resolved by the microCT instrument (voxel size 700^3 nm^3),[116] nevertheless, Figure 5b shows a magnified 3D rendered volume that mostly comprises a NMC-rich pillar, showing some smaller NMC811 particles

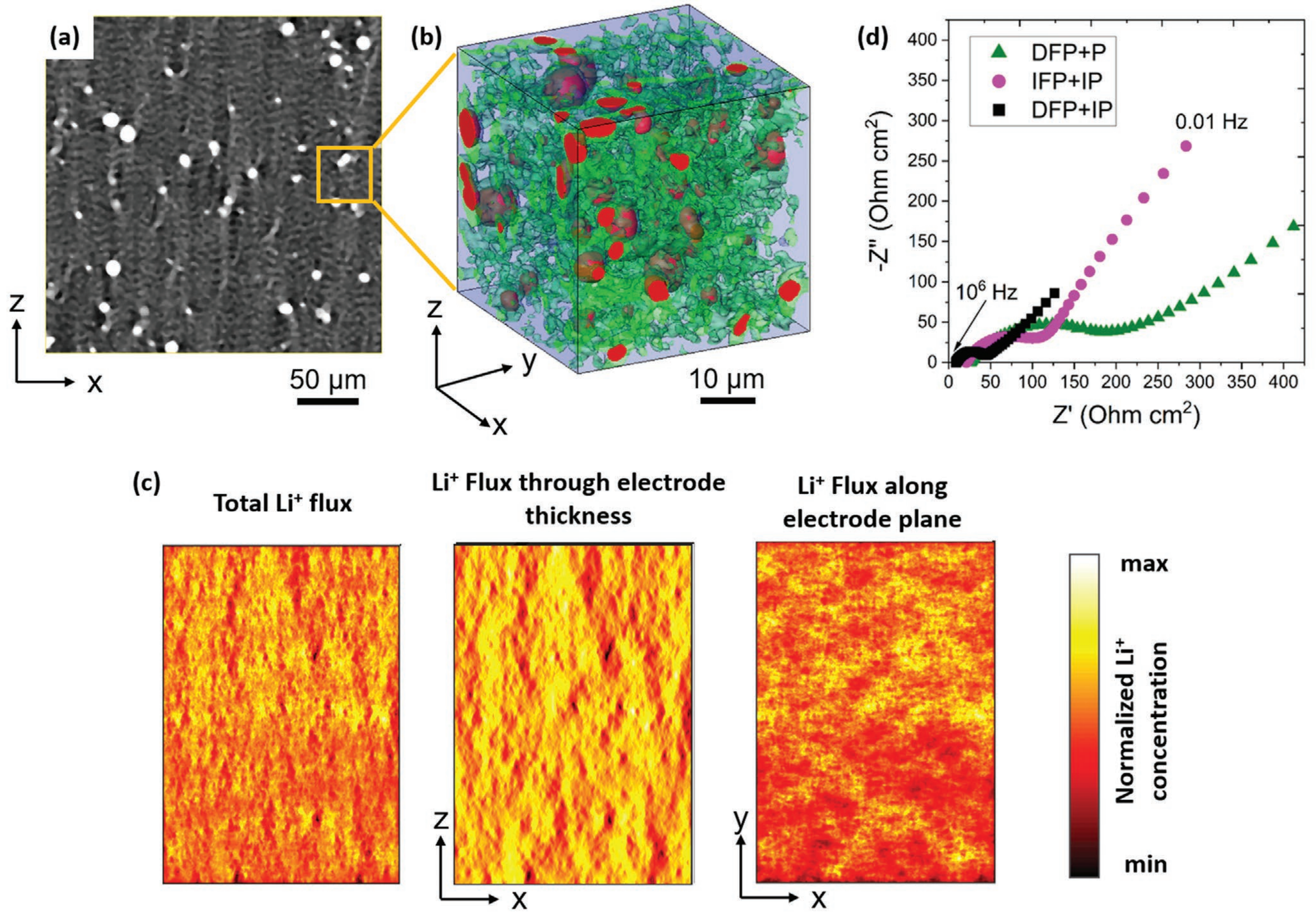

Figure 5. a) A grey-scale 2D slice of a [DFP+IP] cathode from X-ray micro-computed tomography (microCT), b) a segmented 3D volume rendering of a magnified region in (a), c) simulated Li$^+$ ion total flux, flux through electrode thickness and flux along electrode plane of the [DFP+IP] electrode, and d) Nyquist plot of the Li/SSE/cathode full cell using the [DFP+IP], [IFP+IP] and [DFP+P] cathodes.

encapsulated by the SSE and corroborating the cross-sectional SEM images in Figure 3c,d.

To investigate electrode microstructural effects on long-range Li$^+$ ion transport, finite difference method-based ion transport simulations were performed using the segmented microCT data to quantify the orthogonal x–y–z Li$^+$ ion transport fluxes. Li$^+$ ions were simulated moving from one side of the cathode to the other in the x–z plane (i.e., in the direction through the cathode thickness), and then along the x–y plane (i.e., horizontally within the cathode plane) according to a difference in ion concentration imposed on opposite faces of the volume. This approach does not simulate ion mobility during actual charge/discharge but allows quantification of the relative ion mobility in orthogonal directions in a real 3D microstructure.[117] Figure 5c shows the corresponding simulated ion fluxes, showing an 81% increase in the ion flux through the electrode thickness (the preferable ion transport direction during (dis)charge) compared with the ion flux in the electrode plane.

Tortuosity τ was used to quantify the resistance to the Li$^+$ ion flux in orthogonal directions and was obtained by comparing the effective Li$^+$ ion flux through the cathode (F_p) with the idealized Li$^+$ ion flux through a volume of the same size of the cathode (F_{cv}) according to:

$$F_p = -AD\frac{\varepsilon}{\tau}\frac{\Delta C}{L} \tag{1}$$

$$F_{cv} = -AD\frac{\Delta C}{L} \tag{2}$$

where ε is volume fraction of SSE, D is diffusivity of Li$^+$ ions, ΔC is the imposed, starting Li$^+$ ion concentration difference across an electrode thickness L with cross-sectional area A. Hence, τ was estimated from the ratio between F_p and F_{cv} ($\tau = 1$ indicates an idealized straight path.[118]) For the through cathode thickness direction, previous simulations have shown that for $\tau_z > 3$, Li$^+$ ion transport in the cathode is significantly impeded and restricts the realizable capacity of SSLMBs.[52] In practice, $\tau_z = 3.3$ to 4.9 is obtained experimentally for most cathodes (⩽300 µm thick) comprising a conventional randomly mixed microstructure of cathode and SSE materials.[71,118,119] Even for an idealized cathode comprising a randomly mixed microstructure of NMC and $Li_{10}GeP_2S_{12}$ SSE with no microvoids, computational simulations have yielded $\tau_z = 2.3$.[59] In this study, $\tau_z = 5.6$ was estimated for the 600 µm thick [IFP+IP] cathode that reduced significantly to $\tau_z = 1.2$ for the 600 µm thick [DFP+IP] cathode which was comparable with $\tau_z = 1.2$ to 1.9 for cathodes containing anisotropic pore structures for liquid electrolyte-based batteries made by multi-step pore templating methods.[116,120,121]

To explore the microstructural effects on electrode resistance, EIS was used to investigate the [IFP+IP], [DFP+P], and [DFP+IP] cathodes in a cathode/SSE/Li full cell configuration at 25 °C and Figure 5d shows the corresponding Nyquist plots. The intercept of the Nyquist curves with the real *Z*-axis at the highest frequency represents the equivalent series resistance (R_s) of the cathode and the SSE, while the diameter of a best-fit semi-circle to the data represents the charge resistance (R_{CT}) of the cathode and the interfacial resistance between the cathode and SSE.[110] R_s was estimated at 8.9, 21.2, and 31.4 Ω cm^2, and R_{CT} at 37.7, 85.5, and 148.6 Ω cm^2 for the cells using [DFP+IP], [IFP+IP], and [DFP+P] cathodes, respectively. The R_s and R_{CT} for the [DFP+IP] and [IFP+IP] cathodes were lower than for the [DFP+P] cathode due to the better NMC811 particle/SSE contact and higher intrinsic ionic conductivity of [LiTFSI+PEGMA+MePrPyl TFSI] that enabled relatively fast Li$^+$ ion diffusion through the cathode. The [DFP+IP] cathode had both the lowest R_s and R_{CT} because it had the lowest through thickness SSE tortuosity and the C-coated NMC particles were contrived into pillars that improved electrical conductivity. Nonetheless, resistances remained relatively high, as is often the case for SSLMBs, and contriving electron conductivity additives into the NMC-rich pillars might be beneficial, although the active material fraction would have to be proportionally reduced.

The effective Li$^+$ ion diffusivity (D_{eff}) of the [DFP+IP], [IFP+IP], and [DFP+P] cathodes was estimated via DC depolarization experiments in a Li/cathode/Li cell configuration.[121] The cell was first polarized at a low current of 10 µA for 2 h to produce a Li$^+$ ion concentration gradient that was then allowed to relax (depolarize) until the cell potential *V* approached equilibrium (dV/dt < 0.1 mV h^{-1}).[122] Figure S12a–c, Supporting Information shows graphs of $\ln|V(t){-}V(t=\infty)|$ versus time *t* for the three types of cathode. The linear best-fit (red line) to the data suggested that Li$^+$ transport in the electrode was diffusion-limited[123] and so the relaxation time t_{re} was determined from the linear region according to:

$$t_{re} = L^2/(\pi^2 D_{eff}) \tag{3}$$

where *L* is the thickness of the electrode, and $D_{eff} = 1.4 \pm 0.06 \times 10^{-7}$, $8.9 \pm 0.08 \times 10^{-8}$ and $4.4 \pm 1.01 \times 10^{-9}$ cm^2 s^{-1} was estimated for the [DFP+IP], [IFP+IP], and [DFP+P] cathodes, respectively. The ion diffusivity in the [IFP+IP] cathode was consistent with previous reports of 3.1 to 9.1×10^{-8} cm^2 s^{-1} for composite cathodes with a randomly mixed structure of active and an ionic polymer PEO-IL SSE.[124] Overall, X-ray microCT, simulations, EIS, and DC depolarization studies consistently showed that the anisotropic structure improved ion mobility kinetics in the critical through-thickness direction of the [DFP+IP] cathode.

2.5. Electrochemical Properties of SSLMB Full Cells

Figure S13, Supporting Information shows a cyclic voltammogram of a cathode/SSE/Li full cell with a [DFP+IP] hybrid cathode between 2.4 and 4.7 V at a scan rate of 0.1 mV s^{-1}. The maxima of the three largest peaks during charge were at 3.8, 4.0, and 4.2 V, and the three corresponding peaks during discharge were at 3.7, 4.0, and 4.2 V. These peaks relate to changes in Li$^+$ layer spacing and Li$^+$ mobility in the NMC811 crystal structure and consistent with previous work.[88] The EIS results in Figure 5d show the high resistance of the [DFP+P] cathode and no useful capacity was obtained. **Figure 6**a compares the galvanostatic charge and discharge profiles of the SSLMB full cells using the [IFP+IP] and [DFP+IP] cathodes at 0.05 C (assuming the theoretical capacity of NMC811 is 200 mAh g^{-1}[88]), at the first and tenth cycle and 25 °C. The [IFP+IP] cathode delivered discharge capacities of 152 and 149 mAh g^{-1} at the first and tenth cycles, respectively, corresponding to areal capacities of 12.5 and 12.2 mAh cm^{-2}. The [DFP+IP] cathode delivered higher discharge capacities of 199 and 196 mAh g^{-1} at the first and tenth cycles, respectively, corresponding to areal capacities of 16.7 and 16.4 mAh cm^{-2}. Figure S14, Supporting Information shows the corresponding charge and discharge profiles as a function of areal capacity. The gravimetric capacity of the [DFP+IP] cathode was higher than other SSLMB cathodes, for example, 110–120 mAh g^{-1} for $LiMn_2O_4$,[125] 120–160 mAh g^{-1} for $LiCoO_2$,[120,126] 116–162 mAh g^{-1} for $LiFePO_4$,[116,127] 140–170 mAh g^{-1} for $LiMnO_2$,[128,129] 160–170 mAh g^{-1} for $LiNi_{0.33}Mn_{0.33}Co_{0.33}O_2$,[130] and 162–180 mAh g^{-1} for NMC811[131,132] at the same measurement conditions. The high capacity arose from the intrinsic higher capacity of NMC811, the higher ionic conductivity of the [LiTFSI+PEGMA+MePrPyl TFSI] SSE and the higher effective Li$^+$ ion diffusivity in the vertically aligned cathode structure.

The [DFP+IP] cathode areal capacity was also higher than other SSLMB cathodes, for example, 0.2 mAh cm^{-2} for $LiNi_{0.8}Co_{0.15}Al_{0.05}O_2$ cathode with Li_2S-P_2S_5 SSE,[133] 1 mAh cm^{-2} for $LiFePO_4$ cathode with poly(styrene trifluoromethanesulphonylimide of Li) P(STFSILi)-PEO-P(STFSILi) polyanionic block copolymer SSE[134] and 10 mAh cm^{-2} for $LiCoO_2$ cathode with polystyrene-b-poly(4-vinylpyridine) block copolymer and $Li_7La_3Zr_2O_{12}$ composite SSE.[64]

Figure 6b shows the galvanostatic charge and discharge profiles of the [DFP+IP] cathode in a SSLMB full cell with increasing charge and discharge rates from 0.05 to 1 C (1 C ≈ 1 h charge or discharge) at 25 °C. The cell was charged and discharged for five cycles at each increasing C rate, followed by another five cycles at 0.05 C. Rates of ⩽1 C are normally used for relatively thick electrodes in SSLMBs that require current densities 2–20 times higher than used for conventional thickness electrodes (30–300 µm).[31,135–137] Figure S15, Supporting Information shows the corresponding galvanostatic charge and discharge profiles at increasing C rate as a function of areal capacity. Figure 6c summarizes the rate-dependent discharge gravimetric specific capacities of the [DFP+IP] and [IFP+IP] cathodes, with the [DFP+IP] cathode maintaining a higher capacity at all C rates, for example, 120 and 71 mAh g^{-1} (10.1 and 5.8 mAh cm^{-2}) for the [DFP+IP] and [IFP+IP] cathodes, respectively, at 1 C (corresponding discharge areal capacity summary in Figure S16, Supporting Information). The capacity retention was 93% ± 2.1% at 0.1 C, 78% ± 2.0% at 0.5 C, and 63% ± 1.7% at 1 C for the [DFP+IP] cathode, and 89% ± 2.3% at 0.1 C, 68% ± 2.2% at 0.5 C, and 46% ± 1.8% at 1 C for the [IFP+IP] cathode.

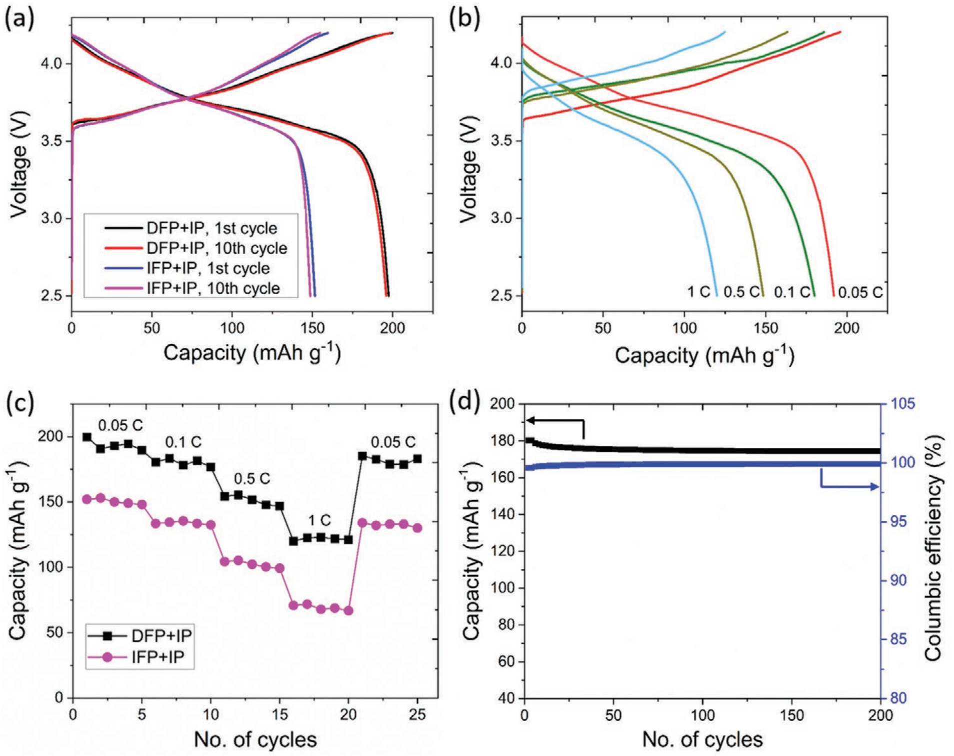

Figure 6. a) Galvanostatic charge and discharge profiles of the [IFP+IP] and [DFP+IP] hybrid cathodes in SSLMB full cells at 0.05 C, b) galvanostatic charge and discharge profiles of the [DFP+IP] cathode in a SSLMB full cell at increasing charge and discharge rates, c) rate capability of the [IFP+IP] and [DFP+IP] cathodes in SSLMB full cells, and d) cycling performance and Coulombic efficiency of the [DFP+IP] cathode at 0.5 C, all at 25 °C.

The composite cathode capacity and performance determines the maximum energy density possible in a SSLMB full cell using Li metal as the anode.[8] The energy density of the full cell E was estimated using $E = VCm/M$ where V is the average voltage of discharge, C is the specific capacity of the cathode, m is the mass of the cathode, and M is the total mass of the full cell including the mass of solid-state electrolyte and Li metal anode.[8] The SSLMB using the [DFP+IP] cathode yielded $E = 301$ Wh kg^{-1} at room temperature, higher than $E = 227$ Wh kg^{-1} using the [IFP+IP] cathode, and also than higher than $E = 232$ Wh kg^{-1} for a solid-state battery comprising a $LiCoO_2$-based cathode, a Ta-substituted $Li_7La_3Zr_2O_{12}$ solid electrolyte and a Li metal anode[63] and $E = 166$ Wh kg^{-1} for a solid-state battery using a $Li_3V_2(PO_4)_3$ cathode, a $Li_{1.3}Al_{0.3}Ti_{1.7}(PO_4)_3$ solid electrolyte and a $LiTi_2(PO_4)_3$ anode.[138] In principle, the energy density of the [DFP+IP] cathode could be further increased by increasing the active material NMC811:SSE ratio, but it anticipated that only marginal gains are achievable before the continuity of the ionic pathways would be undermined.

Finally, Figure 6d shows the discharge capacity and Coulombic efficiency of the [DFP+IP] cathode in a SSLMB full cell during cycling at 0.5 C, showing 94% capacity retention and 97% Coulombic efficiency after 200 cycles. The relatively high cycling performance and Coulombic efficiency were due to the high electrochemical stability of the SSE against the Li metal anode and the mechanical stability conferred by the UV cured ionic polymer, corroborating the LSV results in Figure S11, Supporting Information.

3. Conclusions

We have developed a directional freezing and polymerization (DFP) processing method to fabricate 600 µm thick solid-state lithium metal battery (SSLMB) cathodes with an anisotropic structure containing vertically aligned $LiNi_{0.8}Mn_{0.1}Co_{0.1}O_2$ (NMC811)-rich pillars surrounded by a [PEGMA+MePrPyl TFSI+LiTFSI] polymer composite electrolyte. The DFP method does not require any post-processing steps such as template removal and infiltration that are typically used to make anisotropic structured electrodes. Instead, the anisotropic cathode structure was formed in situ during self-assembly under directional freezing followed by polymerization that provided excellent NMC/SSE contact. DFT calculations, DSC and EIS results showed the [PEGMA+MePrPyl TFSI+LiTFSI] SSE had high electrochemical and thermal stability and a competitive intrinsic ionic conductivity of 4.2×10^{-4} S cm^{-1} at 25 °C. X-ray micro-computed tomography, Li^+ ion transport simulations, and DC depolarization results demonstrated that the vertically aligned cathode structure reduced Li^+ ion transport pathway tortuosity from 3.3 to 4.9 for standard SSLMB composite cathodes to 1.2, and increased effective ion diffusivity from 4.4×10^{-9} to 1.4×10^{-7} cm^2 s^{-1}. SSLMB full cells using the [DFP+IP] hybrid cathode exhibited a near theoretical gravimetric capacity of 199 mAh g^{-1} and a superb areal capacity of 16.7 mAh cm^{-2} at 0.05 C at 25 °C, as well as delivering 120 mAh g^{-1} (10.1 mAh cm^{-2}) at 1 C. The vertically aligned structure allowed efficient use of active material in a practical thick electrode format. The relatively straightforward DFP processing method, and the many potential variants that are readily suggested, may provide new opportunities for scalable SSLMB fabrication routes that more effectively realize the high capacity of thick cathodes in SSLMBs.

4. Experimental Section

Electrode and SSE Fabrication: $LiNi_{0.8}Mn_{0.1}Co_{0.1}O_2$ (NMC811) powder was provided by Targray, UK. A viscous electrode suspension was prepared by mixing the NMC811 powder, lithium bis(trifluoromethylsulfonyl)imide (LiTFSI) salt (Sigma Aldrich, UK), and a photoinitiator Irgacure (Sigma Aldrich, UK) at a weight ratio of 2.5:2:0.5 in a mixture of 1-methyl-1-propylpyrrolidinium bis(trifluoromethanesulfonyl)imide (MePrPyl TFSI) and a monomer solution of poly(ethylene glycol) methacrylate (PEGMA, $M_n = 500$) at a volume ratio of 0.5:1. For the directional freezing and polymerization (DFP) process, the suspension was directionally frozen in a custom-made 3D printed acrylonitrile butadiene styrene (ABS) mould at a freezing rate of 2 mm min^{-1} that was controlled by a heating coil around a copper cold finger, one end of which was immersed in liquid nitrogen. Free-standing frozen electrodes were extracted from the mould and then directly underwent a UV-initiated cryopolymerization (average UV light intensity of 400 mW cm^{-2} at 365 nm) at −25 °C. For comparison, electrodes using the same materials were also fabricated by isotropic freezing and polymerization (IFP) method by placing the electrode suspension in a temperature controlled freezer. To form an electrically insulating SSE membrane on the NMC811-based cathode, a viscous suspension of LiTFSI and Irgacure in a mixture of MePrPyl TFSI and PEGMA was drop cast on the cured cathode, and UV cured at −25 °C. Finally, a Li metal foil was placed on the SSE membrane and the battery was sealed in a CR2032 coin cell in an Ar filled glovebox ($H_2O < 0.1$ ppm, $O_2 < 0.1$ ppm).

Characterization: The NMC811 powder and the resulting electrodes were investigated by X-ray diffraction (XRD, D5000, Siemens) with Cu_α radiation $\lambda = 1.5$ Å. Thermal stability and any phase separation in the cathodes was evaluated using differential scanning calorimetry (DSC, Diamond Hyper, Perkin Elmer) by heating samples at 50 °C min^{-1} from −85 to 300 °C. Cross sections of the electrodes were prepared using a precision etching coating system (PECS 685, Gatan) at an energy of 4 keV Ar^+ beam in vacuum for 2 h. The electrode cross sections were examined by scanning electron microscopy (SEM) and energy dispersive X-ray spectroscopy (EDS) analysis (Merlin Analytical, Zeiss). The electrode particle was examined by transmission electron microscopy (TEM) (Tecnai G^2F20, FEI). X-ray micro-computed tomography (microCT) was performed on the cathode (Xradia Versa530, Zeiss); each scan comprised 3142 2D radiographic projections. The cells were galvanostatically charged and discharged between 2.5 and 4.2 V at different C rates using a battery cycler (BT-G-25, Arbin) at room temperature. Gravimetric capacity was calculated based on the weight of actives with a variance of ±3% over 50 samples of each type. Cyclic voltammetry was performed between 2.3 and 4.7 V at 0.1 mV s^{-1} and electrochemical impedance spectroscopy (EIS) was performed by applying a voltage amplitude of 100 mV at open circuit voltage in the 10^6–0.01 Hz frequency range using a potentiostat/galvanostat (Reference 600/EIS300, Gamry).

Modeling and Image Quantification: The density functional theory (DFT) geometries were optimized for each of the functionals with the 6-31+G(d,p) basis set that considered p-type polarization for hydrogen atoms and d-type polarization and diffuse functions for all other elements, which were important in improving the accuracy of the calculation for soft molecular systems.[139] All microCT scans were reconstructed into a 3D volume using filtered back projection and beam hardening correction algorithms embedded in Scout-and-Scan Control System Reconstructor software. The reconstructed image volumes were post-processed and quantified by Avizo 9.7.0 software. A 3D median filter with a kernel of 3 × 3 × 3 was applied to all image volumes for noise removal.[114] The filtered image volumes were then segmented using the Otsu threshold,[140] resulting in binarized image volumes for analysis. Individual phases from the microCT scans based on $-\ln(I/I_0) = \mu t$ were investigated, where I is the intensity of attenuated X-rays, I_0 is the intensity of incoming X-rays, μ is the mass attenuation coefficient of X-ray, and t is the effective thickness of the phase. Directional tortuosity was estimated using the TauFactor code in MatLab.[117]

Supporting Information

Supporting Information is available from the Wiley Online Library or from the author.

Acknowledgements

This work was supported by an EPSRC UKRI Innovation Fellowship EP/S001239/1 "Novel Manufacturing Approaches to Next Generation Batteries"; the Henry Royce Institute (through EPSRC Grant EP/R010145/1); and the EPSRC Grant EP/M009521/1 "Enabling Next Generation Lithium Batteries". The use of XCT facilities and Avizo license funded by EPSRC Grant EP/M02833X/1 "University of Oxford: experimental equipment upgrade" is gratefully acknowledged. C.L.A.L. is grateful for the EPSRC grant (EP/R511638/1) to work on this project. The authors thank Prof. Peter G. Bruce for the precision etching and coating system (PECS) for sample preparation.

Conflict of Interest

The authors declare no conflict of interest.

Keywords

battery manufacture, cathodes, ion transport, NMC811, solid-state batteries

Received: July 23, 2020
Revised: October 1, 2020

[1] A. W. Schaefer, S. R. H. Barrett, K. Doyme, L. M. Dray, A. R. Gnadt, R. Self, A. O'Sullivan, A. P. Synodinos, A. J. Torija, *Nat. Energy* **2019**, *4*, 160.
[2] X.-B. Cheng, R. Zhang, C.-Z. Zhao, Q. Zhang, *Chem. Rev.* **2017**, *117*, 10403.
[3] J. Liu, Z. Bao, Y. Cui, E. J. Dufek, J. B. Goodenough, P. Khalifah, Q. Li, B. Y. Liaw, P. Liu, A. Manthiram, Y. S. Meng, V. R. Subramanian, M. F. Toney, V. V. Viswanathan, M. S. Whittingham, J. Xiao, W. Xu, J. Yang, X.-Q. Yang, J.-G. Zhang, *Nat. Energy* **2019**, *4*, 180.
[4] Y. Zhang, T.-T. Zuo, J. Popovic, K. Lim, Y.-X. Yin, J. Maier, Y.-G. Guo, *Mater. Today* **2019**, *33*, 56. https://doi.org/10.1016/j.mattod.2019.09.018
[5] K. Xu, *Chem. Rev.* **2014**, *114*, 11503.
[6] Y.-G. Lee, S. Fujiki, C. Jung, N. Suzuki, N. Yashiro, R. Omoda, D.-S. Ko, T. Shiratsuchi, T. Sugimoto, S. Ryu, J. H. Ku, T. Watanabe, Y. Park, Y. Aihara, D. Im, I. T. Han, *Nat. Energy* **2020**, *5*, 299. https://doi.org/10.1038/s41560-020-0575-z
[7] V. Yufit, F. Tariq, D. S. Eastwood, M. Biton, B. Wu, P. D. Lee, N. P. Brandon, *Joule* **2019**, *3*, 485.
[8] S. Randau, D. A. Weber, O. Kotz, R. Koerver, P. Braun, A. Weber, E. Ivers Tiffee, T. Adermann, J. Kulisch, W. G. Zeier, F. H. Ritchter, J. Janek, *Nat. Energy* **2020**, *5*, 259.

[9] J. C. Bachman, S. Muy, A. Grimaud, H.-H. Chang, N. Pour, S. F. Lux, O. Paschos, F. Maglia, S. Lupart, P. Lamp, L. Giordano, Y. Shao-Horn, *Chem. Rev.* **2016**, *116*, 140.
[10] Q. Zhao, S. Stalin, C.-Z. Zhao, L. A. Archer, *Nat. Rev. Mater.* **2020**, *5*, 229.
[11] H. Aono, E. Sugimoto, Y. Sadaoka, N. Imanaka, G.-Y. Adachi, *J. Electrochem. Soc.* **1990**, *137*, 1023.
[12] H. Aono, E. Sugimoto, Y. Sadaoka, N. Imanaka, G.-Y. Adachi, *J. Electrochem. Soc.* **1993**, *140*, 1827.
[13] J. Bu, P. Leung, C. Huang, S. H. Lee, P. S. Grant, *J. Mater. Chem. A* **2019**, *7*, 19094.
[14] V. Thangadurai, W. Weppner, *Adv. Funct. Mater.* **2005**, *15*, 107.
[15] H. Peng, Q. Wu, L. Xiao, *J. Sol-Gel Sci. Technol.* **2013**, *66*, 175.
[16] Y. X. Gao, X. P. Wang, W. G. Wang, Q. F. Fang, *Solid State Ionics* **2010**, *181*, 33.
[17] A. Morata-Orrantia, S. García-Martín, E. Moran, M. A. Alario-Franco, *Chem. Mater.* **2002**, *14*, 2871.
[18] V. Thangadurai, A. K. Shukla, J. Gopalakrishnan, *Chem. Mater.* **1999**, *11*, 835.
[19] M. Itoh, Y. Inaguma, W.-H. Jung, L. Chen, T. Nakamura, *Solid State Ionics* **1994**, *70-71*, 203.
[20] S. Song, J. Lu, F. Zheng, H. M. Duong, L. Lu, *RSC Adv.* **2015**, *5*, 6588.
[21] P. Oh, H. Lee, S. Park, H. Cha, J. Kim, J. Cho, *Adv. Energy Mater.* **2020**, *10*, 2000904.
[22] M. Tachez, J.-P. Malugani, R. Mercier, G. Robert, *Solid State Ionics* **1984**, *14*, 181.
[23] M. Murayama, R. Kanno, M. Irie, S. Ito, T. Hata, N. Sonoyama, Y. Kawamoto, *J. Solid State Chem.* **2002**, *168*, 140.
[24] Y. Deng, C. Eames, J.-N. Chotard, F. Lalere, V. Seznec, S. Emge, O. Pecher, C. P. Grey, C. Masquelier, M. S. Islam, *J. Am. Chem. Soc.* **2015**, *137*, 9136.
[25] S. Boulineau, M. Courty, J.-M. Tarascon, V. Viallet, *Solid State Ionics* **2012**, *221*, 1.
[26] O. Pecher, S.-T. Kong, T. Goebel, V. Nickel, K. Weichert, C. Reiner, H.-J. Deiseroth, J. Maier, F. Haarmann, D. Zahn, *Chem. - Eur. J.* **2010**, *16*, 8347.
[27] H.-J. Deiseroth, J. Maier, K. Weichert, V. Nickel, S.-T. Kong, C. Reiner, *Z. Anorg. Allg. Chem.* **2011**, *637*, 1287.
[28] B. L. Papke, M. A. Ratner, D. F. Shriver, *J. Phys. Chem. Solids* **1981**, *42*, 493.
[29] A. Basile, M. Hilder, F. Makhlooghiazad, C. Pozo Gonzalo, D. R. MacFarlane, P. C. Howlett, M. Forsyth, *Adv. Energy Mater.* **2018**, *8*, 1703491.
[30] S. Isikli, K. M. Ryan, *Curr. Opin. Electrochem.* **2020**, *21*, 188.
[31] J. Wan, J. Xie, X. Kong, Z Liu, K. Liu, F. Shi, A. Pei, H. Chen, W. Chen, J. Chen, X. Zhang, L. Zong, J. Wang, L.-Q. Chen, J. Qin, Y. Cui, *Nat. Nanotech.* **2019**, *14*, 705.
[32] Z. Guo, Y. Zhang, Y. Dong, J. Li, S. Li, P. Shao, X. Feng, B. Wang, *JACS* **2019**, *141*, 1923.
[33] C. Ma, Y. Feng, F. Xing, L. Zhou, Y. Yang, Q. Xia, L. Zhou, L. Zhang, L. Chen, D. G. Ivey, D. R. Sadoway, W. Wei, *J. Mater. Chem. A* **2019**, *7*, 19970.
[34] E. J. Cheng, K. Hong, N. J. Taylor, H. Choe, J. Wolfenstine, J. Sakamoto, *J. Eur. Ceram. Soc.* **2017**, *37*, 3213.
[35] J. Zhou, T. Qian, J. Liu, M. Wang, L. Zhang, C. Yan, *Nano Lett.* **2019**, *19*, 3066.
[36] R. Koerver, W. Zhang, L. de Biasi, S. Schweidler, A. O. Kondrakov, S. Kolling, T. Brezesinski, P. Hartmann, W. G. Zeier, J. Janek, *Energy Environ. Sci.* **2018**, *11*, 2142.
[37] N. V. Ilawe, J. Fu, S. Ramanathan, B. M. Wong, J. Wu, *J. Phys. Chem. C* **2016**, *120*, 27757.
[38] J. M. Pringle, P. C. Howlett, D. R. MacFarlane, M. Forsyth, *J. Mater. Chem.* **2010**, *20*, 2056.
[39] P. Leung, J. Bu, V. P. Quijano, M. R. Roberts, N. Grobert, P. S. Grant, *Adv. Energy Mater.* **2019**, *9*, 1901418.
[40] A. S. Shaplov, R. Marcilla, D. Mecerreyes, *Electrochim. Acta* **2015**, *175*, 18.
[41] T. Ueki, M. Watanabe, *Macromolecules* **2008**, *41*, 3739.
[42] A. Sakuda, A. Hayashi, Y. Takigawa, K. Higashi, M. Tatsumisago, *J. Ceram. Soc. Jpn.* **2013**, *121*, 946.
[43] J. H. Lee, C. S. Yoon, J.-Y. Hwang, S.-J. Kim, F. Maglia, P. Lamp, S.-T. Myungd, Y.-K. Sun, *Energy Environ. Sci.* **2016**, *9*, 2152.
[44] C. Stetson, T. Yoon, J. Coyle, W. Nemeth, M. Young, A. Norman, S. Pylypenko, C. Ban, C.-S. Jiang, M. Al-Jassim, A. Burrell, *Nano Energy* **2019**, *55*, 477.
[45] J. Ma, J. Sung, Y. Lee, Y. Son, S. Chae, N. Kim, S.-H. Choi, J. Cho, *Adv. Energy Mater.* **2020**, *10*, 1903400.
[46] K.-H. Chen, A. J. Sanchez, E. Kazyak, A. L. Davis, N. P. Dasgupta, *Adv. Energy Mater.* **2019**, *9*, 1802534.
[47] X. Zhang, R. Lv, A. Wang, W. Guo, X. Liu, J. Luo, *Angew. Chem., Int. Ed.* **2018**, *57*, 15028.
[48] Q. Li, S. Zhu, Y. Lu, *Adv. Funct. Mater.* **2017**, *27*, 1606422.
[49] C. Niu, H. Pan, W. Xu, J. Xiao, J.-G. Zhang, L. Luo, C. Wang, D. Mei, J. Meng, X. Wang, Z. Liu, L. Mai, J. Liu, *Nat. Nanotechnol.* **2019**, *14*, 594.
[50] C.-H. Chen, F. Brosa Planella, K. O'Regan, D. Gastol, W. D. Widanage, E. Kendrick, *J. Electrochem. Soc.* **2020**, *167*, 080534.
[51] C. Yang, K. Fu, Y. Zhang, E. Hitz, L. Hu, *Adv. Mater.* **2017**, *29*, 1701169.
[52] A. Bielefeld, D. A. Weber, J. Janek, *J. Phys. Chem. C* **2019**, *123*, 1626.
[53] S. Xu, K.-H. Chen, N. P. Dasgupta, J. B. Siegel, A. G. Stefanopoulou, *J. Electrochem. Soc.* **2019**, *166*, A3456.
[54] R. Drummond, C. Huang, P. S. Grant, S. R. Duncan, *J. Power Sources* **2019**, *433*, 126579.
[55] M. Ebner, D.-W. Chung, R. E. Garcia, V. Wood, *Adv. Energy Mater.* **2014**, *4*, 1301278.
[56] T. Huria, G. Ludovici, G. Lutzemberger, *J. Power Sources* **2014**, *249*, 92.
[57] K. G. Gallagher, S. E. Trask, C. Bauer, T. Woehrle, S. F. Lux, M. Tschech, P. Lamp, B. J. Polzin, S. Ha, B. Long, Q. Wu, W. Lu, D. W. Dees, A. N. Jansen, *J. Electrochem. Soc.* **2015**, *163*, A138.
[58] L. Froboese, J. Felix van der Sichel, T. Loellhoeffel, L. Helmers, A. Kwade, *J. Electrochem. Soc.* **2019**, *166*, A318.
[59] Y. Kato, S. Shiotani, K. Morita, K. Suzuki, M. Hirayama, R. Kanno, *J. Phys. Chem. Lett.* **2018**, *9*, 607.
[60] S.-J. Choi, S.-H. Choi, A. D. Bui, Y.-J. Lee, S.-M. Lee, H.-C. Shin, Y.-C. Ha, *ACS Appl. Mater. Interfaces* **2018**, *10*, 31404.
[61] M. Yamamoto, Y. Terauchi, A. Sakuda, M. Takahashi, *Sci. Rep.* **2018**, *8*, 1212.
[62] M. A. Kraft, S. Ohno, T. Zinkevich, R. Koerver, S. P. Culver, T. Fuchs, A. Senyshyn, S. Indris, B. J. Morgan, W. G. Zeier, *J. Am. Chem. Soc.* **2018**, *140*, 16330.
[63] M. Finsterbusch, T. Danner, C.-L. Tsai, S. Uhlenbruck, A. Latz, O. Guillon, *ACS Appl. Mater. Interfaces* **2018**, *10*, 22329.
[64] H. Wakayama, H. Yonekura, Y. Kawai, *Chem. Mater.* **2016**, *28*, 4453.
[65] C. Mao, R. E. Ruther, J. Li, Z. Du, I. Belharouak, *Electrochem. Commun.* **2018**, *97*, 37.
[66] M. Wetjen, G.-T. Kim, M. Joost, G. B. Appetecchi, M. Winter, S. Passerini, *J. Power Sources* **2014**, *246*, 846.
[67] D. H. Kim, D. Y. Oh, K. H. Park, Y. E. Choi, Y. J. Nam, H. A. Lee, S.-M. Lee, Y. S. Jung, *Nano Lett.* **2017**, *17*, 3013.
[68] K. Nie, Y. Hong, J. Qiu, Q. Li, X. Yu, H. Li, L. Chen, *Front. Chem.* **2018**, *6*, 616.
[69] S. Zekoll, C. M. Edwards, A. K. O. Hekselman, J. Kasemchainan, C. Kuss, D. E. J. Armstrong, D. Cai, R. J. Wallace, F. H. Richter, J. H. J. Thijssen, P. G. Bruce, *EES* **2018**, *11*, 185.

[70] G. Shao, D. A. H. Hanaor, X. Shen, A. Gurlo, *Adv. Mater.* **2020**, *32*, 1907176.
[71] S. R. Daemi, X. Lu, D. Sykes, J. Behnsen, C. Tan, A. Palacios-Padros, J. Cookson, E. Petrucco, P. J. Withers, D. J. L. Brett, P. R. Shearing, *Mater. Horiz.* **2019**, *6*, 612.
[72] G. C. Sosso, J. Chen, S. J. Cox, M. Fitzner, P. Pedevilla, A. Zen, A. Michaelides, *Chem. Rev.* **2016**, *116*, 7078.
[73] J. D. Stevenson, P. G. Wolynes, *J. Phys. Chem. A* **2011**, *115*, 3713.
[74] M. Forsyth, L. Porcarelli, X. Wang, N. Goujon, D. Mecerreyes, *Acc. Chem. Res.* **2019**, *52*, 686.
[75] P. Garra, C. Dietlin, F. Morlet-Savary, F. Dumur, D. Gigmes, J.-P. Fouassier, J. Lalevée, *Polym. Chem.* **2017**, *8*, 7088.
[76] M. Bouzrati-Zerelli, J. Kirschner, C. P. Fik, M. Maier, C. Dietlin, F. Morlet-Savary, J. P. Fouassier, J.-M. Becht, J. E. Klee, J. Lalevée, *Macromolecules* **2017**, *50*, 6911.
[77] H.-J. Ha, Y. H. Kwon, J. Y. Kim, S.-Y. Lee, *Electrochim. Acta* **2011**, *57*, 40.
[78] C.-J. Bae, C. K. Erdonmez, J. W. Halloran, Y.-M. Chiang, *Adv. Mater.* **2013**, *25*, 1254.
[79] J. S. Sander, R. M. Erb, L. Li, A. Gurijala, Y.-M. Chiang, *Nat. Energy* **2016**, *1*, 1.
[80] S. Behr, R. Amin, Y.-M. Chiang, A. P. Tomsia, *Ceram. Forum Inter.* **2015**, *92*, 39.
[81] Y. Yang, Q. Wu, D. Wang, C. Ma, Z. Chen, C. Zhu, Y. Gao, C. Li, *J. Membr. Sci.* **2020**, *595*, 117549.
[82] V. Gregorio, N. García, P. Tiemblo, *Membrane* **2019**, *9*, 50. https://doi.org/10.3390/membranes9040050.
[83] R. He, T. Kyu, *Macromolecules* **2016**, *49*, 5637.
[84] M. Taghavikish, S. Subianto, Y. Gu, X. Sun, X. S. Zhao, N. R. Choudhury, *Sci. Rep.* **2018**, *8*, 10918.
[85] X. Wang, H. Zhu, G. M. A. Girard, R. Yunis, D. R. MacFarlane, D. Mecerreyes, A. J. Bhattacharyya, P. C. Howlett, M. Forsyth, *J. Mater. Chem. A* **2017**, *45*, 23844.
[86] F. Hippauf, B. Schumm, S. Doerfler, H. Althues, S. Fujiki, T. Shiratsuchi, T. Tsujimura, Y. Aihara, S. Kaskel, *Energy Storage Mater.* **2019**, *21*, 390.
[87] A. Sakuda, A. Hayashi, T. Ohtomo, S. Hama, M. Tatsumisago, *J. Power Sources* **2011**, *196*, 6735.
[88] K. Märker, P. J. Reeves, C. Xu, K. J. Griffith, C. P. Grey, *Chem. Mater.* **2019**, *31*, 2545.
[89] M. Wang, Y. Gong, Y. Gu, Y. Chen, L. Chen, H. Shi, *Ceram.* **2019**, *45*, 3177.
[90] W. Li, J. N. Reimers, J. R. Dahn, *Solid State Ionics* **1993**, *67*, 123.
[91] G. B. Appetecchi, G.-T. Kim, M. Montanino, M. Carewska, R. Marcilla, D. Mecerreyes, I. De Meatza, *J. Power Sources* **2010**, *195*, 3668.
[92] T. M. M. Heenan, A. V. Llewellyn, A. S. Leach, M. D. R. Kok, C. Tan, R. Jervis, D. J. L. Brett, P. R. Shearing, *Adv. Sci.* **2010**, *7*, 2000362.
[93] H. Sun, K. Zhao, *J. Phys. Chem. C* **2017**, *121*, 6002.
[94] H.-J. Noh, S. Youn, C. S. Yoon, Y.-K. Sun, *J. Power Sources* **2013**, *233*, 121.
[95] C. Yang, X. Zhang, M. Huang, J. Huang, Z. Fang, *ACS Appl. Mater. Interfaces* **2017**, *9*, 12408.
[96] X. Judez, G. G. Eshetu, C. Li, L. M. Rodriguez-Martinez, H. Zhang, M. Armand, *Joule* **2018**, *2*, 2208.
[97] T. Eliades, W. A. Brantley, *Orthodontic Applications of Biomaterials*, Woodhead Publishing, Amsterdam, The Netherlands **2017**.
[98] S. K. Chaurasia, A. Chandra, *Solid State Ionics* **2017**, *307*, 35.
[99] C. L. Davidson, A. J. Feilzer, *J. Dent.* **1997**, *25*, 435.
[100] K. C. Kim, T. Liu, S. W. Lee, S. S. Jang, *JACS* **2016**, *138*, 2374.
[101] M. Namazian, H. A. Almodarresieh, M. R. Noorbala, H. R. Zare, *Chem. Phys. Lett.* **2004**, *396*, 424.
[102] S. Kazemiabnavi, Z. Zhang, K. Thornton, S. Banerjee, *J. Phys. Chem. B* **2016**, *120*, 5691.
[103] Y. X. Qiu, D. Klee, W. pluster, B. Severich, H. Hocker, *J. Appl. Polymer Sci.* **1996**, *61*, 2373.
[104] M. P. S. Mousavi, B. E. Wilson, Sadra. Kashefolgheta, E. L. Anderson, S. He, P. Buhlmann, A. Stein, *ACS Appl. Mater. Interfaces* **2016**, *8*, 3396.
[105] P. Peljo, H. H. Girault, *EES* **2018**, *11*, 2306.
[106] M. Ebadi, C. Marchiori, J. Mindemark, D. Brandell, C. M. Araujo, *J. Mater. Chem. A* **2019**, *7*, 8394.
[107] J. Liang, Y. Sun, Y. Zhao, Q. Sun, J. Luo, F. Zhao, X. Lin, X. Li, R. Li, L. Zhang, S. Lu, H. Huang, X. Sun, *J. Mater. Chem. A* **2020**, *8*, 2769.
[108] M. Zaheer, H. Xu, B. Wang, L. Li, Y. Deng, *J. Electrochem. Soc.* **2020**, *167*, 070504.
[109] S. Menkin, M. Lifshitz, A. Haimovic, hM. Goor, R. Blanga, S. G. Greenbaum, A. Goldbourt, D. Golodnitsky, *Electrochim. Acta* **2019**, *304*, 447.
[110] J. Ou, G. Li, Z. Chen, *J. Electrochem. Soc.* **2019**, *166*, A1785.
[111] C. Li, X. Zheng, Y. Pan, Q. Y. Li, *ACS Appl. Mater. Interfaces* **2019**, *11*, 34904.
[112] N. Goujon, T. Huynh, R. Kerr, K. Vezzu, V. Di Noto, J. Chiefari, P. C. Howlett, M. Forsyth, *Batteries Supercaps* **2019**, *2*, 132.
[113] S. Mogurampelly, J. R. Keith, V. Ganesan, *JACS* **2017**, *139*, 9511.
[114] C. L. A. Leung, R. Tosi, E. Muzangaza, S. Nonni, P. J. Withers, P. D. Lee, *Mater. Des.* **2019**, *174*, 107792.
[115] L. Almar, J. Joos, A. Weber, E. Ivers-Tiee, *J. Power Sources* **2019**, *427*, 1.
[116] C. Huang, M. Dontigny, K. Zaghib, P. S. Grant, *J. Mater. Chem. A* **2019**, *7*, 21421.
[117] S. J. Cooper, A. Bertei, P. R. Shearing, J. A. Kilner, N. P. Brandon, *Software X* **2016**, *5*, 203.
[118] S. J. Cooper, D. S. Eastwood, J. Gelb, G. Damblanc, D. J. L. Brett, R. S. Bradley, P. J. Withers, P. D. Lee, A. J. Marquis, N. P. Brandon, P. R. Shearing, *J. Power Sources* **2014**, *247*, 1033.
[119] C. Tan, S. R. Daemi, O. O. Taiwo, T. M. M. Heenan, D. J. L. Brett, P. R. Shearing, *Materials* **2018**, *11*, 2157.
[120] C. Huang, P. S. Grant, *J. Mater. Chem. A* **2018**, *6*, 14689.
[121] L. Li, R. M. Erb, J. Wang, J. Wang, Y.-M. Chiang, *Adv. Energy Mater.* **2018**, *9*, 1802472.
[122] Z. Osman, M. I. M. Ghazali, L. Othman, K. B. M. Isa, *Results Phys.* **2012**, *1*, 4.
[123] I. V. Thorat, D. E. Stephenson, N. A. Zacharias, K. Zaghib, J. N. Harb, D. R. Wheeler, *J. Power Sources* **2009**, *188*, 592.
[124] J.-H. Shin, W. A. Henderson, S. Passerini, *J. Electrochem. Soc.* **2005**, *152*, A978.
[125] D. Guyomard, J. M. Tarascon, *J. Electrochem. Soc.* **1992**, *139*, 937.
[126] N. Nitta, F. Wu, J. T. Lee, G. Yushin, *Mater. Today* **2015**, *18*, 252.
[127] M. S. Islam, C. A. J. Fisher, *Chem. Soc. Rev.* **2014**, *43*, 185.
[128] I. Koetschau, M. N. Richard, J. R. Dahn, J. B. Soupart, J. C. Rousche, *J. Electrochem. Soc.* **1995**, *142*, 2906.
[129] P. G. Bruce, A. R. Armstrong, R. L. Gitzendanner, *J. Mater. Chem.* **1999**, *9*, 193.
[130] F. Lin, I. M. Markus, D. Nordlund, T.-C. Weng, M. D. Asta, H. L. Xin, M. M. Doeff, *Nat. Commun.* **2014**, *5*, 3529.
[131] L. Yue, J. Ma, J. Zhang, J. Zhao, S. Dong, Z. Liu, G. Cui, L. Chen, *Energy Storage Mater.* **2016**, *5*, 139.
[132] F. Baskoro, H. Q. Wong, H.-J. Yen, *ACS Appl. Energy Mater.* **2019**, *2*, 3937.
[133] U. Ulissi, M. Agostini, S. Ito, Y. Aihara, J. Hassoun, *Solid State Ionics* **2016**, *296*, 13.
[134] R. Bouchet, S. Maria, R. Meziane, A. Aboulaich, L. Lienafa, J.-P. Bonnet, T. N. T. Phan, D. Bertin, D. Gigmes, D. Devaux, R. Denoyel, M. Armand, *Nat. Mater.* **2013**, *12*, 452.
[135] E. Fedeli, O. Garcia-Calvo, T. Thieu, T. N. T. Phan, D. Gigmes, I. Urdampilleta, A. Kvasa, *Electrochim. Acta* **2020**, *353*, 136481.

[136] M. D. Widstrom, K. B. Ludwig, J. E. Matthews, A. Jarry, M. Erdi, A. V. Cresce, G. Rubloff, P. Kofinas, *Electrochim. Acta* **2020**, *345*, 136156.
[137] G. Homann, L. Stolz, J. Nair, I. C. Laskovic, M. Winter, J. Kasnatscheew, *Sci. Rep.* **2020**, *10*, 4390.
[138] S. Yu, A. Mertens, H. Tempel, R. Schierholz, H. Kungl, R.-A. Eichel, *ACS Appl. Mater. Interfaces* **2018**, *10*, 22264.
[139] S. Zahn, D. R. MacFarlane, E. I. Izgorodina, *Phys. Chem. Chem. Phys.* **2013**, *15*, 13664.
[140] N. Otsu, *IEEE Trans. Syst. Man. Cybern.* **1979**, *9*, 62.